materials

MDPI

Article

Mechanical and Dielectric Properties of Two Types of Si_3N_4 Fibers Annealed at Elevated Temperatures

Jie Zhou, Fang Ye, Xuefeng Cui, Laifei Cheng *, Jianping Li, Yongsheng Liu and Litong Zhang

Science and Technology on Thermostructural Composite Materials Laboratory, Northwestern Polytechnical University, Xi'an 710072, China; 13628013651@163.com (J.Z.); yefang511@nwpu.edu.cn (F.Y.); cuixuefeng@nwpu.edu.cn (X.C.); ijianping@163.com (J.L.); yongshengliu@nwpu.edu.cn (Y.L.); zhanglt@nwpu.edu.cn (L.Z.)

* Correspondence: chenglf@nwpu.edu.cn

Received: 5 July 2018; Accepted: 14 August 2018; Published: 22 August 2018

Abstract: The mechanical and dielectric properties of two types of amorphous silicon nitride (Si_3N_4) fibers prior to and following annealing at 800 °C were studied. The tensile strengths of the Si_3N_4 fiber bundles were measured using unidirectional tensile experimentation at room temperature, whereas the permittivity values were measured at 8.2–12.4 GHz using the waveguide method. The results demonstrated that the tensile strength and dielectric properties of Si_3N_4 fibers were correlated to the corresponding composition, microstructure, and intrinsic performance of electrical resistance. The Si_3N_4 fibers with a lower content of amorphous SiN_xO_y presented an improved thermal stability, a higher tensile strength, a higher conductivity, and a significantly stable wave-transparent property. These were mainly attributed to the highly pure composition and decomposition of less amorphous SiN_xO_y.

Keywords: Si_3N_4 fiber; wave-transparent; thermal stability; mechanical properties; dielectric properties

1. Introduction

Radome [1,2], as an indispensable part of high-performance missile weapons, plays a vital role in the normal operation of these weapons. In order that the missile weapons function in harsh environments, the performance required for wave-transparent materials under high temperature is increasingly demanding [3–6]. Silicon nitride (Si_3N_4), which demonstrates high strength, good thermal shock resistance, wear resistance, outstanding oxidation resistance, and chemical stability characteristics, is increasingly studied and applied as a high-temperature structural ceramic [7–11]. In addition, Si_3N_4 ceramics possess a low dielectric constant and a high electrical resistivity, which are the preferred properties for the transmission and insulation of electromagnetic waves in high-temperature environments [12–16]. Furthermore, Si_3N_4 nanomaterials, another hotspot of research, have both the advantages of Si_3N_4 and nanomaterials, which could be used to prepare nanofluids possessing different properties than their solids [17,18]. The continuous Si_3N_4 ceramic fiber is a new type of high-performance ceramic fiber, developed on the basis of precursor-converted continuous SiC ceramic fibers [19–21]. As a type of Si_3N_4 material, it has a series of excellent properties, proving to be a popular reinforced material candidate for high-temperature wave-transparent ceramic matrix composites (CMCs) used in radomes [21,22].

Considering the Si_3N_4 fiber as a core reinforcement material for radomes, there are strict requirements to follow regarding the mechanical and dielectric properties. Ideally, low and stable dielectric constant (ε) and dielectric loss (tan δ) are required in addition to the necessary mechanical properties, generally with values not exceeding 4.0 and 0.01 [23,24], respectively. During preparation, the fiber composition can differ due to different conditions, which affect it directly, consequently

affecting the corresponding microscopic structure and performance [25,26]. In this study, two types of Si_3N_4 fibers were heat treated at 800 °C, while the composition, microstructure, tensile strength, complex permittivity ($\varepsilon_r = \varepsilon' - \varepsilon''j$), and dielectric loss ($\tan\delta = \varepsilon''/\varepsilon'$) of both Si_3N_4 fibers, in the as-received and heat-treated states, were investigated in detail.

2. Experimentation

2.1. Materials and Heat Treatments

The materials selected for experimentation were two different types of Si_3N_4 fiber bundles, supplied by Xiamen University of China, each consisting of 500 filaments, and woven into two-dimensional cloths by the Shaanxi Institute of Textile Science. The as-received Si_3N_4 fibers were produced by the pyrolysis of polycarbosilane (PCS). Because of the different pyrolysis conditions during preparation, the test results showed that the most significant difference between the two types of fibers was the oxygen content. For the convenience of subsequent description, the Si_3N_4 fiber with the relatively low oxygen content of 3.56 wt % (determined by a CONS elemental analyzer) was termed as Si_3N_4 fiber-L; the Si_3N_4 fiber with the relatively high oxygen content of 13.56 wt %, corresponded to Si_3N_4 fiber-H. In order to analyze the preparation temperature of the composites toughened by the Si_3N_4 fibers to see whether it had an effect on the characteristic performance of the fibers, the Si_3N_4 fibers and fiber cloths were placed in a furnace for chemical vapor decomposition (CVD) without gas at the temperature of 800 °C for up to 2 h of heat treatment, to simulate the preparation environment [27].

2.2. Microstructure Characterization

The surface and cross-section morphology of the Si_3N_4 fibers were analyzed using scanning electron microscopy (SEM) (S4700, Hitachi, Tokyo, Japan). The phase compositions of the Si_3N_4 fibers were analyzed using X-ray diffraction (XRD) (X' Pert Pro, Philips, Amsterdam, The Netherlands) with Cu Kα (λ = 1.54 Å) radiation. The surface composition and chemical bonding states of the Si_3N_4 fibers were measured using X-ray photoelectron spectroscopy (XPS) (Axis Ultra, Oxford, UK). The fiber microstructure and crystalline state were accurately described using transmission electron microscopy (TEM) (G-20, FEI-Tecnai, Hillsboro, OR, USA). The heat treatment behavior of the as-received fibers was determined using thermogravimetric (TG) and differential scanning calorimeter (DSC) analysis (STA 449C, Selb, Germany) under Ar atmosphere at the heating rate of 10 °C/min to a maximum of 800 °C.

2.3. Property Characterization

The unidirectional tensile strengths at room temperature of the fiber bundles were tested. The two ends of the bundles were fixed on a steel plate with an adhesive of 50 mm in gauge length and of 0.2 mm/min in cross-head draw speed. This process was sufficiently slow, to simulate a quasi-static loading. Figure 1 presents the schematic illustration of a tensile specimen for single fiber bundles.

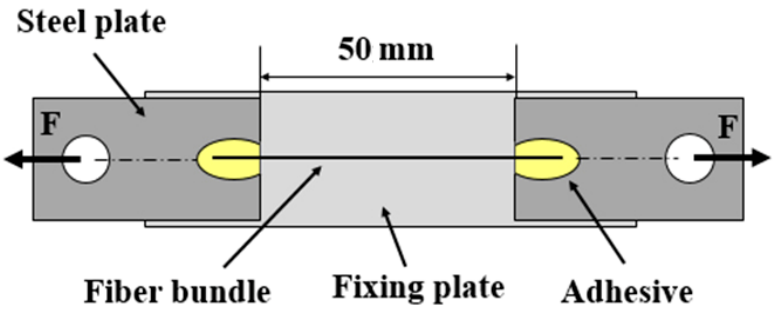

Figure 1. Schematic illustration of tensile specimen for single fiber bundles.

The electrical resistance of fiber bundles was tested with DC sources (6220, Keithley, Cleveland, OH, USA). Silver paste was added as coating on both ends of the fiber bundles to ensure a good electrical contact. The voltage values were determined by the corresponding current values, whereas the average value of resistance (R) was obtained using Ohm's law. The average resistivity of each bundle of fibers (μ) was calculated through the following equation:

$$\mu = \frac{RS}{l}, \quad (1)$$

where S and l are the cross-sectional area and length of the fiber bundles, respectively. The relative complex permittivity testing of Si_3N_4 fibers was conducted using a vector network analyzer (VNA) (MS4644A, Anritsu, Atsugi, Japan), with the waveguide method in the frequency band of 8.2–12.4 GHz. To ensure that the Si_3N_4 fibers could be fixed to facilitate the measurement of dielectric property, the Si_3N_4 fabrics, produced from Si_3N_4 fiber-L and Si_3N_4 fiber-H, were respectively composited with epoxy resin (68 vol %) to obtain fiber/resin composites (named as samples 1 and 2, respectively). To prevent the corresponding effects on the conductivity and dielectric properties, the surface sizing agents on both types of original Si_3N_4 fibers were first removed by water soaking at 80 °C for a period longer than 0.5 h.

3. Results and Discussion

3.1. Microstructure and Composition of As-Received Fibers

Table 1 presents the fundamental characteristics of the Si_3N_4 fibers. The O and C contents of the Si_3N_4 fiber-H were higher, whereas the corresponding mechanical properties were closer to the precursor state [28].

Table 1. Fundamental characteristics of the silicon nitride (Si_3N_4) fibers.

Materials	Element/wt %				Diameter/μm
	Si	N	O	C	
Si_3N_4 fiber-L	59.79	36.0	3.56	0.65	12.2
Si_3N_4 fiber-H	52.39	33.14	13.56	0.91	13

Figure 2 presents the surface morphology and element mapping of both desized Si_3N_4 fibers. The surfaces of both fibers (see Figure 2a,b) were smooth and flat without apparent defects, with no distinct difference between them. It was observed that both fibers displayed relatively uniform diameters of approximately 12.2 μm and 13 μm, respectively. The element mapping (see Figure 2c–f) presented the uniform distributions of Si, N, O, and C.

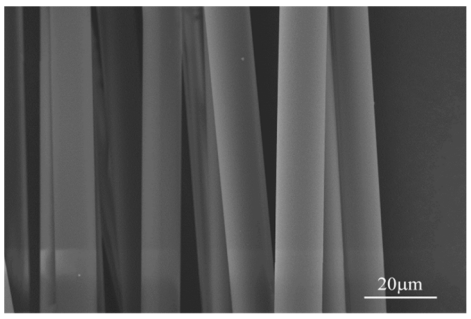

(**a**)

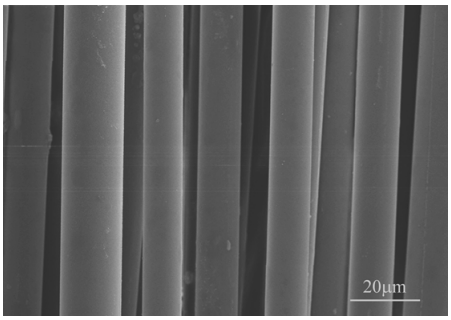

(**b**)

Figure 2. *Cont.*

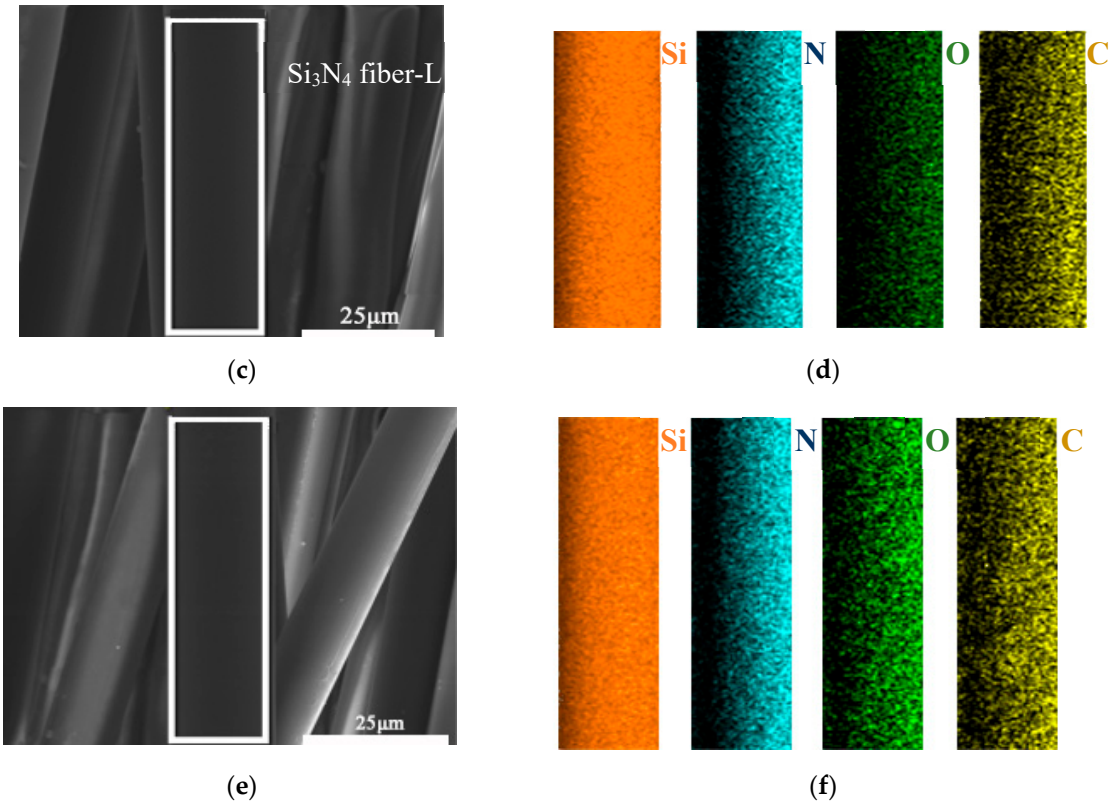

Figure 2. (**a**) Surface SEM images of Si_3N_4 fiber-L and (**b**) Si_3N_4 fiber-H, (**c**,**d**) scanning electron microscopy and energy dispersive pectroscopy (SEM-EDS) element mapping of Si_3N_4 fiber-L and (**e**,**f**) Si_3N_4 fiber-H.

The crystalline states of the untreated fibers and the heat-treated fibers at 800 °C are presented in Figure 3. No apparent crystal absorption peak were noted and only two broad diffraction peaks at approximately 23° and 69° were found in the typical XRD patterns of the two Si_3N_4 fibers annealed at 800 °C under vacuum. This revealed that the heat-treated fibers at 800 °C did not reach the crystallization temperature, remaining in the original amorphous state. High-resolution transmission electron microscopy (HR-TEM) combined with selected-area electron diffraction (SAED) were used to observe the detailed microstructures of both untreated Si_3N_4 fibers.

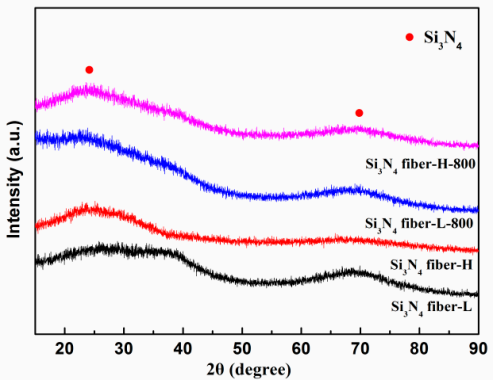

Figure 3. *Cont*.

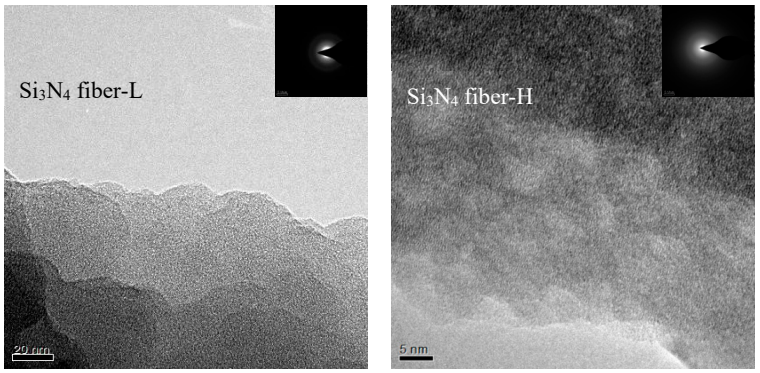

(**b**) (**c**)

Figure 3. (**a**) X-ray diffraction (XRD) patterns of Si_3N_4 fibers prior to and following heat treatment and (**b**,**c**) transmission electron microscopy (TEM) patterns of untreated fibers.

The XPS analyses of both desized fibers were performed to determine the corresponding surface composition and chemical bonding state. In the survey XPS spectra, presented in Figure 4a, the Si 2s, Si 2p, N 1s, C 1s and O 1s peaks were detected. As presented in Figure 4b, two peaks existed in the Si 2p spectrum: one peak was located at 101.8 eV and could be attributed to the Si–O bonds in the SiOx and SiN_xO_y phases, whereas the other peak was located at 101.2 eV, due to Si_3N_4, where the Si–O bond occupied a higher proportion on the Si_3N_4 fiber-H surface compared to the Si_3N_4 fiber-L. Similarly, two peaks existed in the N 1s spectrum, as presented in Figure 4c: one peak was located at 397.0 eV and could be attributed to the N–Si bond, whereas the other peak was located at 398.2 eV due to the N–Si–O bond, which was offered by the SiN_xO_y phase [29]. Furthermore, the O 1s spectrum presented in Figure 4d displayed two peaks. The lower energy peak was located at 532.9 eV, which corresponded well with the O–Si bond value. In addition, the higher energy peak located at 531.6 eV indicated the existence of COx at the fiber surface. At the Si_3N_4 fiber-H surface, a higher proportion of O–Si bond existed from the SiN_xO_y phase. In Figure 4e, C–C bonds, corresponding to the peak located at 284.6 eV, and C–O bonds existed for both fibers. The peak was located at 286.2 eV, where the two bonds originated from the surface sizing agent on the fibers. Considering the existence of NH_3 in the fiber preparation environment, the possibility of a SiN_xO_y phase is much higher than that of a SiO_x one, following Reactions (2) and (3) [30]. Based on the latter analysis, it could be concluded that the two fibers were mainly composed of amorphous Si_3N_4, with low amounts of SiO_x and SiN_xO_y phases.

$$SiO_2(s) + H_2(g) = SiO(g) + H_2O(g), \quad (2)$$

$$SiO(g) + NH_3(g) = SiN_xO_y(g) + H_2O(g) + H_2(g), \quad (3)$$

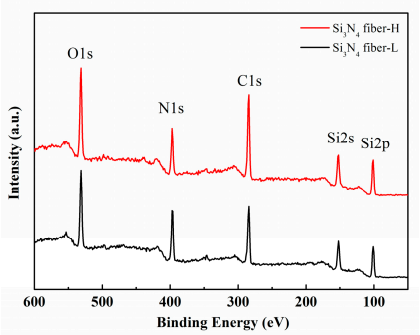

(**a**)

Figure 4. *Cont.*

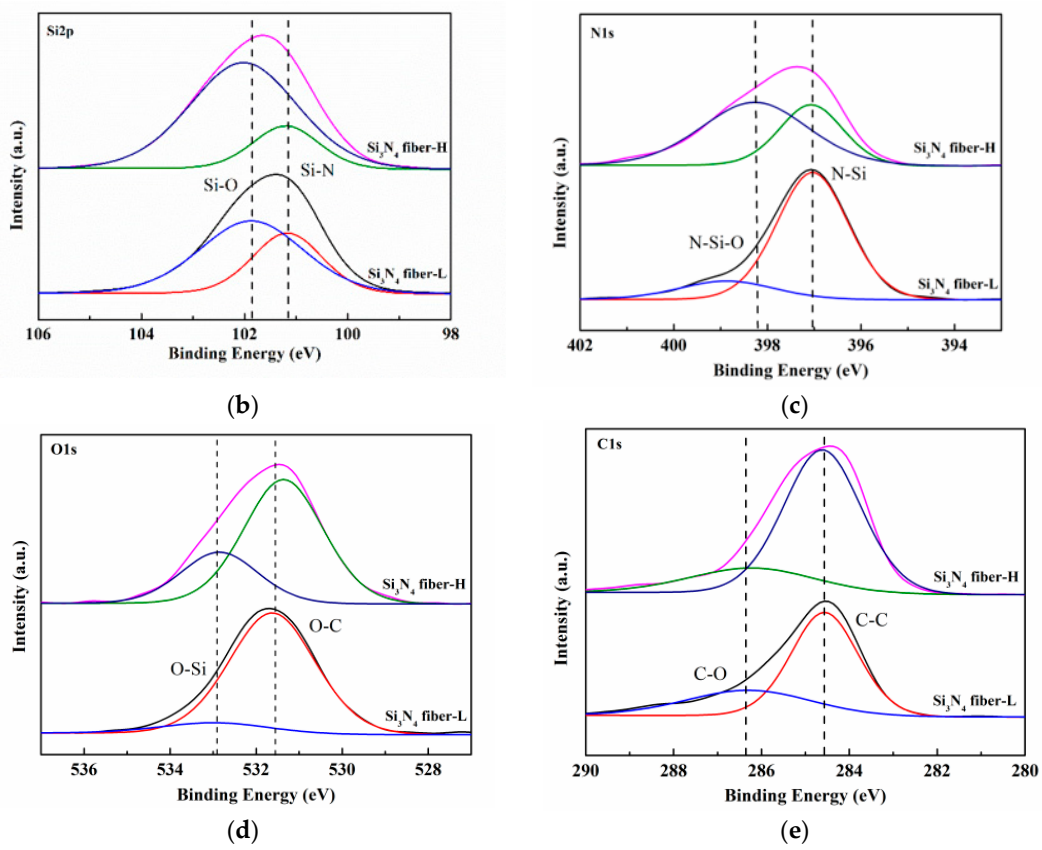

Figure 4. (**a**) XPS survey spectra, (**b**) Si 2p, (**c**) N 1s, (**d**) O 1s, and (**e**) C 1s core level spectra recorded from two desized fibers.

3.2. *Effects of Heat Treatment on Microstructure and Composition*

The element content of both Si_3N_4 fibers following annealing are presented in Table 2. Compared with Table 1, the mass percentage of N elements in both fibers decreased significantly after heat treatment, which may be due to the SiN_xO_y phase decomposition, following Reaction (4) [31].

$$SiN_xO_y(s) = SiO(g) + N_2(g), \quad (4)$$

Table 2. Elemental analysis of Si_3N_4 fibers following annealing.

Materials	Element/wt %			
	Si	N	O	C
Si_3N_4 fiber-L	66.97	27.23	5.12	0.68
Si_3N_4 fiber-H	64.26	25.68	9.24	0.82

The TG-DSC plots of the two as-received fibers are presented in Figure 5. For both fibers, endothermic peaks appeared at approximately 561 °C along with a weight decrease prior to reaching that temperature, which corresponded to the sizing agent decompositions on the fiber surfaces. Adversely, the heat flow curve significantly dropped at approximately 750 °C and its quality had a downward trend for the Si_3N_4 fiber-H. This meant that another endothermic reaction would start to occur, which could be associated with the SiN_xO_y phase decomposition. Because of the negligible content during the SiN_xO_y phase, the SiN_xO_y decomposition caused almost no impact on the Si_3N_4 fiber-L.

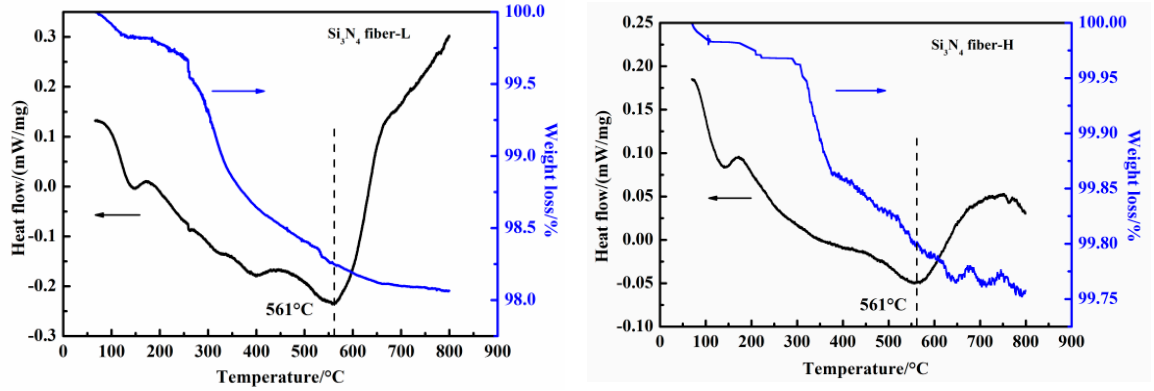

Figure 5. Thermogravimetric and differential scanning calorimeter (TG-DSC) plots of two as-received fibers under Ar atmosphere.

The surface and cross-section morphology (insets) of the two types of desized fibers prior to and following heat treatment are presented in Figure 6, respectively. It was clear that the effect of heat treatment at 800 °C on the microstructure could be observed. Following heat treatment, the surfaces of both fibers changed from smooth and flat to rough. This occurred mainly due to the SiN_xO_y decomposition, affecting the fibers' performances. Moreover, a typical brittle fracture model could be observed from the cross-section morphology. The characteristic mirror, mist, and hackle features were clearly evident in these micrographs [32]. From the crack propagation path, it was observed that the crack source was mainly from the surface flaws for the heat-treated fibers.

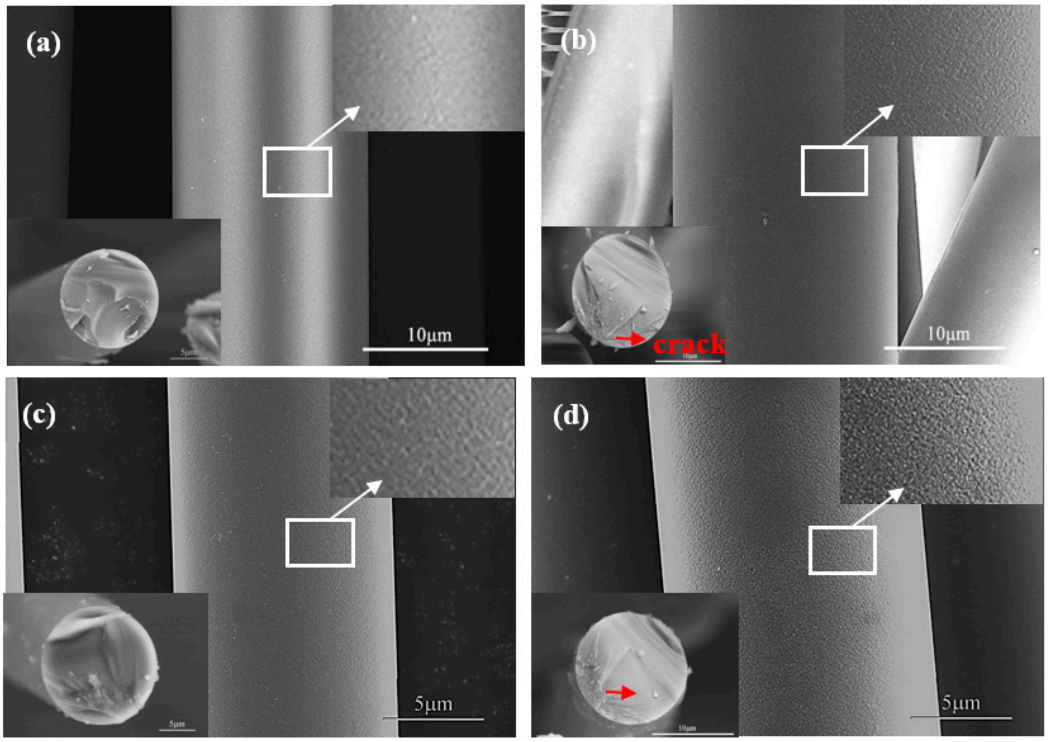

Figure 6. Surface and cross-section (insets) morphologies of (**a**,**b**) Si_3N_4 fiber-L and (**c**,**d**) Si_3N_4 fiber-H prior to and following heat treatment.

In order to verify the SiN_xO_y phase decomposition at the Si_3N_4 fiber-H surface, the corresponding surface chemical bonding states prior to and following annealing were analyzed using XPS. The (a) survey

XPS spectra, (b) Si 2p, and (c) N 1s core level spectra are presented in Figure 7. Compared to the initial Si_3N_4 fiber-H, it was clear that the ratio of Si–O bond to Si–N bond had almost no change following annealing. This occurred because the heat treatment at 800 °C had little effect on the SiO_x phase. In contrast, the N–Si–O bond had a significant reduction following annealing, as the main reason for the amount increase in surface defects, which proved the SiN_xO_y phase decomposition.

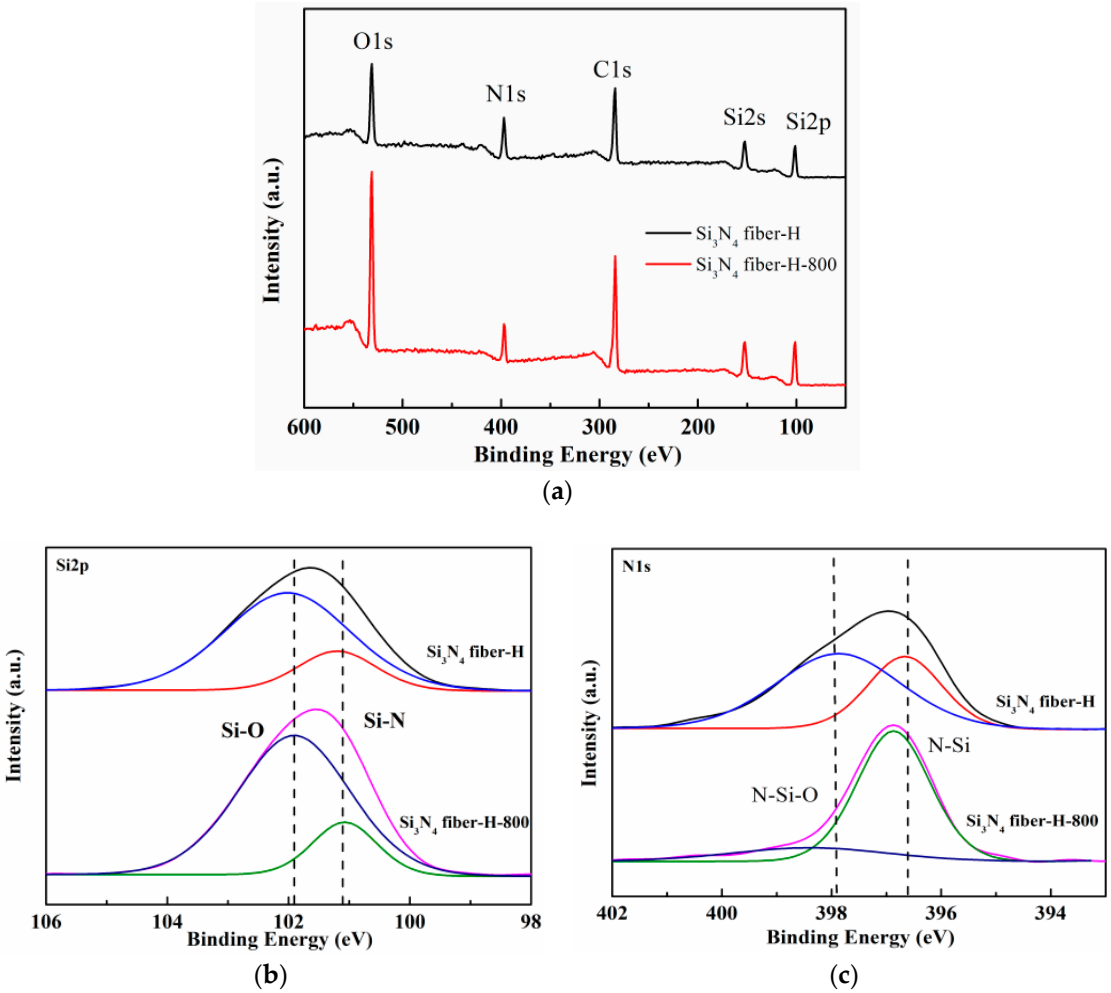

Figure 7. (**a**) XPS survey spectra, (**b**) Si 2p, and (**c**) N 1s core level spectra recorded from Si_3N_4 fiber-H prior to and following annealing.

3.3. Effect of Heat Treatment on Room-Temperature Tensile Strength

The tensile strengths of fibers were measured using the fiber bundle tensile strength measurements. The corresponding dispersions could be well described using the Weibull distribution with two parameters [29]. Figure 8 presents the typical experimental load-displacement curve of the fiber bundles. Figure 8 shows that the fiber bundles were elastically deformed before breaking and that the elastic modulus was constant. Almost all filaments followed a simultaneous fracture behavior when the load reached its maximum, proving that the fiber bundle testing was reasonable. Moreover, a drop point and a post-failure "tail" region were noted. The former was the shake result of the testing equipment, whereas the latter occurred due to friction among neighboring filaments failing at different relative positions. These were not considered for the Weibull parameter calculation in this paper [33].

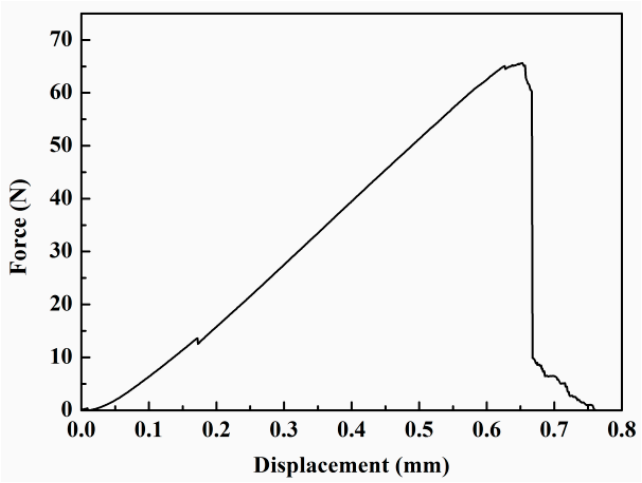

Figure 8. Typical experimental load-displacement curve of the fiber bundles, presenting simultaneous fracture behaviors.

The two-parameter Weibull function is given as follows [34]:

$$F = 1 - \exp[-(\frac{\sigma_i}{\sigma_0})^m], \quad (5)$$

where F is the fracture probability of the fiber under a uniaxial tensile stress σ_i, which is defined as fracture strength. σ_0 and m are the Weibull scale parameter and the Weibull modulus, respectively. As the value of m becomes higher, the strength distribution range becomes narrower and the function curve becomes steeper. Both depend only on the value of m.

The following formula can be obtained, after taking two times the logarithm of Equation (5):

$$\ln\ln\left(\frac{1}{1-S}\right) = m\ln\sigma_i - m\ln\sigma_0, \quad (6)$$

where S is the fracture probability from experiments and can be defined according to Equation (7):

$$S_i = \frac{i - 0.5}{n}, \quad (7)$$

where n is the sample number and i is the rank of σ_i. When the sample size was approximately 10, the S_i was in a weighted analysis [35]. It was apparent that the $\ln\ln(1/(1-S))$ and $\ln\sigma_i$ had a linear correlation, in which the slope was equal to m and the intercept of $\ln\ln(1/(1-S))$ axis was equal to $-m\ln\sigma_0$. Therefore, the values of m and σ_0 could be derived from the experimental data and graphical relationships between $\ln\ln(1/(1-S))$ and $\ln\sigma_i$.

Table 3 lists the Weibull statistics and tensile strength of the two types of Si_3N_4 fiber bundles annealed under vacuum.

Table 3. Comparisons of Weibull statistics and tensile strength of two Si_3N_4 fiber bundles annealed under vacuum.

Materials	Temperature/°C	Weibull Modulus	Scale Parameter/MPa	Tensile Strength/MPa
Si_3N_4 fiber-L	as-received	17.80	1137.9	1104.4
	800	13.31	1142.2	1098.7
Si_3N_4 fiber-H	as-received	13.92	866.8	835.0
	800	13.45	663.1	638.0

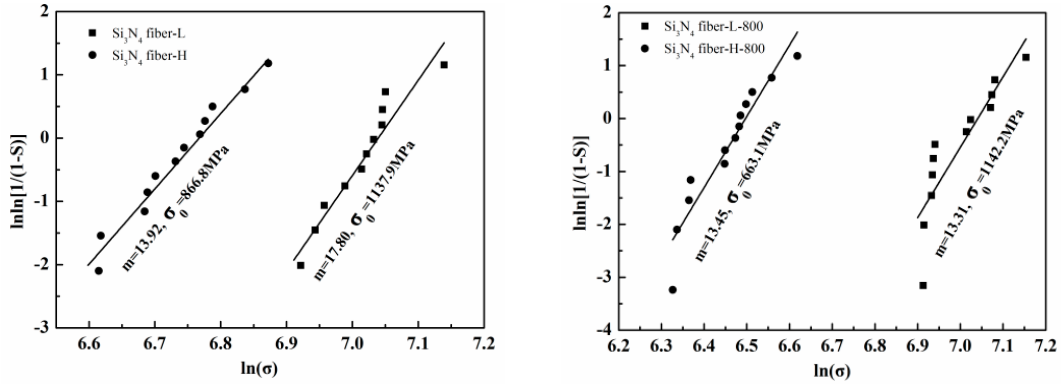

Figure 9. Weibull plots for fiber bundle tests with and without heat treatment.

Figure 9 presents the linear fitting of the relationship between $\ln\ln(1/(1-F))$ and $\ln\sigma_i$ of the two Si_3N_4 fiber bundles. It was clear that the Weibull plots were evenly distributed on both sides of the fitted line, which indicated that the tensile strengths of the fiber bundles followed the two-parameter Weibull distribution.

Figure 10 presents the tensile test results combined with Table 3 and Figure 9. For the as-received fibers, the Si_3N_4 fiber-L strength was 1104.4 MPa, exceeding the 825 MPa reached by the Si_3N_4 fiber-H. In addition, compared to the Si_3N_4 fiber-H, the Si_3N_4 fiber-L had a higher Weibull modulus, which might be attributed to the neater arrangement and fewer internal flaws of filaments, where more filaments could evenly bear load and fracture at the same time, leading to higher strength and more centralized data. Following annealing at 800 °C under vacuum, the strength retention rate of the Si_3N_4 fiber-L was almost 100%, proving that the heat treatment at 800 °C had no effect on its structure, while the value of m decreased from 17.8 to 13.31. This occurred because the fiber bundles scattered and the filaments could be uniformly loaded, mainly due to the sizing agent removal on the fiber surface. The tensile experimentation results demonstrated that the Si_3N_4 fiber-L following heat treatment at 800 °C could still maintain good tensile properties. Adversely, the Si_3N_4 fiber-H tensile strength decreased from 835 MPa to 638 MPa, while the value of m was almost constant following heat treatment, demonstrating that the filaments of the as-received Si_3N_4 fiber-H had a high dispersion by nature. The strength retention result of only 76% indicated that the heat treatment at 800 °C caused damage due to the SiN_xO_y phase decomposition, resulting in a roughened and more defective surface of the Si_3N_4 fiber-H microstructure. This was consistent with the information presented in Figure 6.

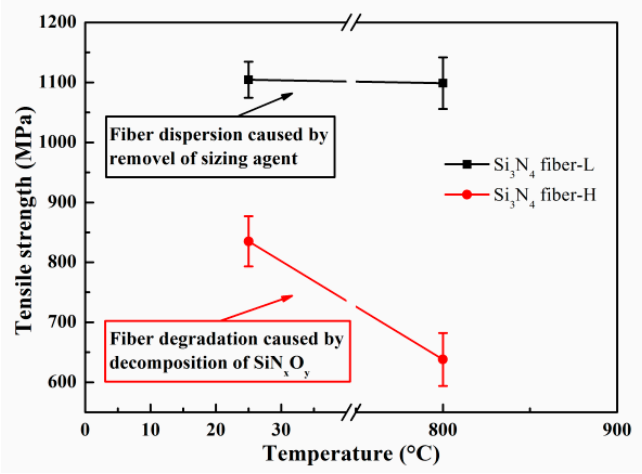

Figure 10. Single tow tensile test results.

According to the research by Taylor [32], a relationship exists among the different diameters of fibers and their strength. As mentioned above, the Si_3N_4 fiber-H diameter was higher. Because of the size effect, the probability of existing defects in the Si_3N_4 fiber-H was higher, which led to a lower and more dispersive strength. Furthermore, a higher content of SiN_xO_y phase was noted, resulting from the Si_3N_4 fiber-H impurities, which were unstable and would be destroyed, while bringing flaws and reducing performance at a high temperature. These could be indirectly proved from Figure 6, demonstrating that the Si_3N_4 fiber-L had improved mechanical properties and high thermal stability.

3.4. Effect of Heat Treatment on Room-Temperature Dielectric Properties

In addition to mechanical properties, the complex permittivity ($\varepsilon = \varepsilon' - j\varepsilon''$) is also an important performance parameter for wave-transparent applications. Figure 11 presents the real part (ε') of permittivity, the imaginary part (ε'') of permittivity, and the dielectric loss (tan δ) of samples 1 and 2 as a function of frequency prior to and following annealing at 800 °C. The ε', ε'' and tan δ at 10 GHz of sample 1 were 3.43, 0.12, and 3.6×10^{-2}, respectively; for sample 2, the corresponding values were 3.18, 0.19, and 5.9×10^{-2}, respectively. Following annealing at 800 °C, these results became 3.19, 0.03, and 9.6×10^{-2} for sample 1, respectively, whereas for sample 2, these results became 2.76, 0.16, and 5.6×10^{-2}, respectively. The fiber/resin composites displayed a low increase of ε' and ε'' compared to the epoxy resin ($\varepsilon'_{resin} = 2.72$, $\varepsilon''_{resin} = 0.07$), due to the conductive behaviors of the Si_3N_4 fibers. The permittivity of the fiber/resin composites, especially for Si_3N_4 fiber-H, presented an apparent frequency dependence, which was one of the features of a dielectric material [36].

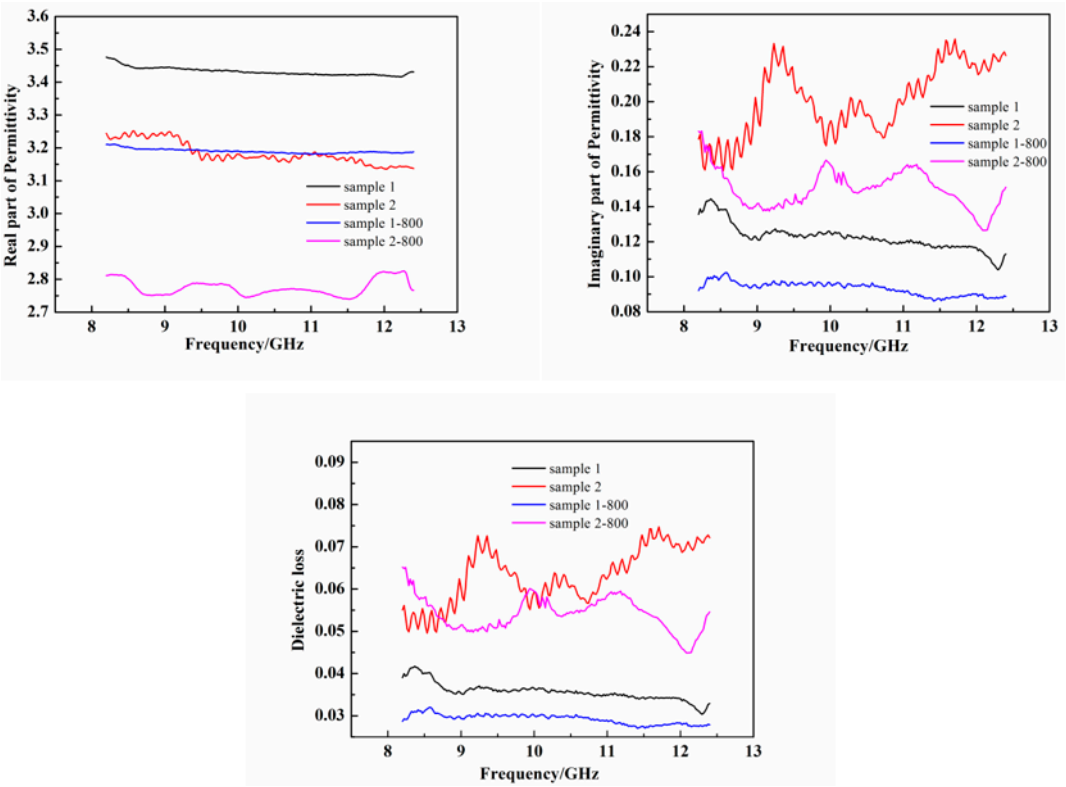

Figure 11. Dielectric properties of two fiber/resin composites in X-band, prior to and following annealing.

It is known that the real part of permittivity is related to the polarization effects and that the imaginary part is related to the electrical conductivity [25,37]. In the Si_3N_4 fiber, the Si_3N_4 was a polar molecule, becoming the dipole under an applied electric field. Under that field, the dipolar polarized and the dipolar polarization was a relaxation, presenting long relaxation time and attenuating high

amount of energy [24]. The Si_3N_4 fiber-L with a higher content of Si_3N_4 had a higher ε', which implied that it possessed a stronger polarization ability.

For dielectric materials, the electrical conductivity (σ) is related to its dielectric property, which can be evaluated through the following equation [38]:

$$\sigma\varepsilon''(\omega) = \omega\varepsilon_0\varepsilon''(\omega), \quad (8)$$

where σ is the electrical conductivity, ε_0 is the free space permittivity ($\varepsilon_0 = 8.854 \times 10^{-12}$ F/m), and ω is the angular frequency. The resistivity and conductivity values of both fibers, prior to and following annealing, are presented in Table 4. Compared to the Si_3N_4 fiber-L, the Si_3N_4 fiber-H had a higher conductivity, which might be attributed to the highly electrical conductive phase of SiN_xO_y compared to the Si_3N_4. The relationships between the imaginary part and conductivity of two Si_3N_4 fibers corresponded reasonably with Equation (6). It is known that the dielectric constant and dielectric loss decrease as the porosity increases [39]. This was caused by the SiN_xO_y decomposition following annealing at 800 °C. Consequently, both fibers annealed at 800 °C had lower dielectric constant and dielectric loss compared to the as-received fibers.

Table 4. Resistivity and conductivity of two fibers prior to and following annealing.

	As-Received		Following Annealing	
Materials	**μ/Ω m**	**σ/S m^{-1}**	**μ/Ω m**	**σ/S m^{-1}**
Si_3N_4 fiber-L	18.94	0.0528	24.29	0.0412
Si_3N_4 fiber-H	31.17	0.0321	33.39	0.0299

4. Conclusions

For the two types of Si_3N_4 fibers studied in this work, the microstructure, the mechanical properties and the dielectric properties were investigated prior to and following heat treatment at 800 °C under vacuum. The microstructural analysis demonstrated that both fibers consisted of amorphous Si_3N_4, as well as SiO_x and SiN_xO_y phases. In addition, the Si_3N_4 fiber-H possessed a higher amount of SiN_xO_y phase. Compared to the Si_3N_4 fiber-H, the Si_3N_4 fiber-L had a higher tensile strength and an improved thermal stability, as a result of its purer component. Following heat treatment, apparent defects and porous surface structures were noted in the Si_3N_4 fiber-H, leading to degradation due to the amorphous SiN_xO_y phase decomposition. Moreover, the Si_3N_4 fiber-L had a higher permittivity and conductivity, resulting in its better polarization ability. Furthermore, the complex permittivity decrease of the annealed Si_3N_4 fiber/epoxy composites was also related to the SiN_xO_y decomposition. The relatively higher strength, the better thermal stability and the same excellent dielectric properties indicated that the Si_3N_4 fiber-L possessed a high serving life at a serving temperature of at least 800 °C. This work could also contribute to the coordination of different service requirements and preparation processes and the selection of high-temperature wave-transparent materials for a potential application in ceramic matrix composites in harsh environments.

Author Contributions: Conceptualization, L.C.; data curation, J.Z. and J.L.; formal analysis, J.Z. and F.Y.; funding acquisition, F.Y., L.C., Y.L., and L.Z.; investigation, X.C.

Funding: This research was funded by the Chinese National Foundation for Natural Sciences under Contracts (Grant No. 51632007) and the Nature Science Foundation of China (Grants: 51602258, 51672217, and 51472201).

Acknowledgments: The authors wish to thank Xiamen University for the supply of Si_3N_4 fibers used in experimentation presented in this paper.

Conflicts of Interest: The authors declare no conflict of interest.

References

1. Mani, G.S. Radome materials. In *Microwave Materials*; Murthy, V.R.K., Sundaram, S., Viswanathan, B., Eds.; Springer: Berlin/Heidelberg, Germany, 1994; pp. 200–239.
2. Gilbert, D.E.; Lee, J.R.; Kramer, T.J. Multilayer Radome. U.S. Patent 4,180,605, 25 December 1979.
3. Barta, J.; Manela, M.; Fischer, R. Si_3N_4 and Si_2N_2O for high performance radomes. *Mater. Sci. Eng.* **1985**, *71*, 265–272. [CrossRef]
4. Suzdal'tsev, E.I.; Kharitonov, D.V.; Anashkina, A.A. Analysis of existing radioparent refractory materials, composites and technology for creating high-speed rocket radomes. Part 2. Comparative analysis of the main properties of materials used for creating rocket radomes. *Refract. Ind. Ceram.* **2010**, *51*, 283–288. [CrossRef]
5. Kim, P.C.; Lee, D.G.; Seo, I.S.; Kim, G.H. Low-observable radomes composed of composite sandwich constructions and frequency selective surfaces. *Compos. Sci. Technol.* **2008**, *68*, 2163–2170. [CrossRef]
6. Place, T.M. Low Loss Radar Window for Reentry Vehicle. U.S. Patent 4,786,548, 22 November 1988.
7. Penas, O.; Zenati, R.; Dubois, J.; Fantozzi, G. Processing, microstructure, mechanical properties of Si_3N_4 obtained by slip casting and pressureless sintering. *Ceram. Int.* **2001**, *27*, 591–596. [CrossRef]
8. Ziegler, A.; Idrobo, J.C.; Cinibulk, M.K.; Kisielowski, C.; Browning, N.D.; Ritchie, R.O. Interface structure and atomic bonding characteristics in silicon nitride ceramics. *Science* **2004**, *306*, 1768–1770. [CrossRef] [PubMed]
9. Dai, J.; Li, J.; Chen, Y.; Yang, L. Effect of the residual phases in β-si_3n_4 seed on the mechanical properties of self-reinforced si_3n_4 ceramics. *J. Eur. Ceram. Soc.* **2003**, *23*, 1543–1547. [CrossRef]
10. Verzemnieks, J.; Simpson, F.H. Silicon Nitride Articles with Controlled Multi-Density Regions. U.S. Patent 5,103,239, 7 April 1992.
11. Chen, F.; Shen, Q.; Zhang, L. Electromagnetic optimal design and preparation of broadband ceramic radome material with graded porous structure. *Prog. Electromagn. Res.* **2010**, *105*, 445–461. [CrossRef]
12. Krstic, Z.; Krstic, V.D. Silicon nitride: The engineering material of the future. *J. Mater. Sci.* **2012**, *47*, 535–552. [CrossRef]
13. Riley, F.L. Silicon nitride and related materials. *J. Am. Ceram. Soc.* **2010**, *83*, 245–265. [CrossRef]
14. Klemm, H. Silicon nitride for high-temperature applications. *J. Am. Ceram. Soc.* **2010**, *93*, 1501–1522. [CrossRef]
15. Miyazaki, H.; Yoshizawa, Y.-I.; Hirao, K. Fabrication of high thermal-conductive silicon nitride ceramics with low dielectric loss. *Mater. Sci. Eng. B* **2009**, *161*, 198–201. [CrossRef]
16. Li, J.Q.; Luo, F.; Zhu, D.M.; Zhou, W.C. Influence of phase formation on dielectric properties of Si_3N_4 ceramics. *J. Am. Ceram. Soc.* **2007**, *90*, 1950–1952. [CrossRef]
17. Żyła, G.; Vallejo, J.P.; Lugo, L. Isobaric heat capacity and density of ethylene glycol based nanofluids containing various nitride nanoparticle types: An experimental study. *J. Mol. Liquids* **2018**, *261*, 530–539. [CrossRef]
18. Żyła, G.; Fal, J.; Bikić, S.; Wanic, M. Ethylene glycol based silicon nitride nanofluids: An experimental study on their thermophysical, electrical and optical properties. *Phys. E Low-Dimens. Syst. Nanostruct.* **2018**, *104*, 82–90. [CrossRef]
19. Chollon, G.; Pailler, R.; Naslain, R.; Laanani, F.; Monthioux, M.; Olry, P. Thermal stability of a pcs-derived sic fibre with a low oxygen content (hi-nicalon). *J. Mater. Sci.* **1997**, *32*, 327–347. [CrossRef]
20. Okamura, K.; Sato, M.; Hasegawa, Y. Silicon nitride fibers and silicon oxynitride fibers obtained by the nitridation of polycarbosilane. *Ceram. Int.* **1987**, *13*, 55–61. [CrossRef]
21. Kamimura, S.; Seguchi, T.; Okamura, K. Development of silicon nitride fiber from si-containing polymer by radiation curing and its application. *Radiat. Phys. Chem.* **1999**, *54*, 575–581. [CrossRef]
22. Pavarajarn, V.; Precharyutasin, R.; Praserthdam, P. Synthesis of silicon nitride fibers by the carbothermal reduction and nitridation of rice husk ash. *J. Am. Ceram. Soc.* **2010**, *93*, 973–979. [CrossRef]
23. Li, X.; Yin, X.; Zhang, L.; Cheng, L.; Qi, Y. Mechanical and dielectric properties of porous Si_3N_4–SiO_2 composite ceramics. *Mater. Sci. Eng. A* **2009**, *500*, 63–69. [CrossRef]
24. Kingery, W.D.; Bowen, H.K.; Uhlmann, D.R. *Introduction to Ceramics*, 2nd ed.; Springer: Tokyo, Japan, 1976.
25. Ye, F.; Zhang, L.; Yin, X.; Liu, Y.; Cheng, L. Dielectric and electromagnetic wave absorbing properties of two types of sic fibres with different compositions. *J. Mater. Sci. Technol.* **2013**, *29*, 55–58. [CrossRef]
26. Chu, Z.; Feng, C.; Song, Y. Effect of oxygen content on tensile strength of polymer-derived sic fibers. *Trans. Nonferrous Met. Soc. China* **2002**, *12*, 894–898.

27. Liu, Y.; Cheng, L.; Zhang, L.; Hua, Y.; Yang, W. Microstructure and properties of particle reinforced silicon carbide and silicon nitride ceramic matrix composites prepared by chemical vapor infiltration. *Mater. Sci. Eng. A* **2008**, *475*, 217–223. [CrossRef]
28. Lin, L.; Xia, W.L.; Chen, J.M.; Ling, L.; Ding, S.N.; Liu, A.H. Preparation of silicon nitride fibers by pyrolysis nitridation of polycarbosilance. *J. Funct. Mater.* **2013**, *44*, 2981–2984.
29. Sun, X.; Liu, H.T.; Cheng, H.F. Oxidation behavior of silicon nitride fibers obtained from polycarbosilane fibers via electron beam irradiation curing. *RSC Adv.* **2017**, *7*, 47833–47839. [CrossRef]
30. Chollon, G.; Vogt, U.; Berroth, K. Processing and characterization of an amorphous Si–N–(O) fibre. *J. Mater. Sci.* **1998**, *33*, 1529–1540. [CrossRef]
31. Singhal, S.C. Thermodynamic analysis of the high-temperature stability of silicon nitride and silicon carbide. *Ceramur. Int.* **1976**, *2*, 123–130. [CrossRef]
32. Taylor, S.T.; Zhu, Y.T.; Blumenthal, W.R.; Stout, M.G.; Butt, D.P.; Lowe, T.C. Characterization of nicalon fibres with varying diameters: Part i strength and fracture studies. *J. Mater. Sci.* **1998**, *33*, 1465–1473. [CrossRef]
33. Dassios, K.G.; Steen, M.; Filiou, C. Mechanical properties of alumina nextel™ 720 fibres at room and elevated temperatures: Tensile bundle testing. *Mater. Sci. Eng. A* **2003**, *349*, 63–72. [CrossRef]
34. Wolfenden, A.; van der Zwaag, S. The concept of filament strength and the weibull modulus. *J. Test. Eval.* **1989**, *17*, 292–298. [CrossRef]
35. Riccardi, C.C.; Vallo, C.I. Estimation of weibull parameters for the flexural strength of pmma-based bone cements. *Polym. Eng. Sci.* **2002**, *42*, 1260–1273. [CrossRef]
36. Wang, G.; Chen, X.; Duan, Y.; Liu, S. Electromagnetic properties of carbon black and barium titanate composite materials. *J. Alloys Compd.* **2008**, *454*, 340–346. [CrossRef]
37. Yin, X.; Xue, Y.; Zhang, L.; Cheng, L. Dielectric, electromagnetic absorption and interference shielding properties of porous yttria-stabilized zirconia/silicon carbide composites. *Ceram. Int.* **2012**, *38*, 2421–2427. [CrossRef]
38. Wen, B.; Cao, M.S.; Hou, Z.L.; Song, W.L.; Zhang, L.; Lu, M.M.; Jin, H.B.; Fang, X.Y.; Wang, W.Z.; Yuan, J. Temperature dependent microwave attenuation behavior for carbon-nanotube/silica composites. *Carbon* **2013**, *65*, 124–139. [CrossRef]
39. Jia, D.; Shao, Y.; Liu, B.; Yu, Z. Characterization of porous silicon nitride/silicon oxynitride composite ceramics produced by sol infiltration. *Mater. Chem. Phys.* **2010**, *124*, 97–101. [CrossRef]